Flying shape and aerodynamics of a full-scale flexible Olympic windsurf sail

Jishen Zhang[a], Gauthier Bertrand[a], Marc Rabaud[b], Benoît Augier[c], Marc Fermigier[a,*]

[a]*Physique et Mécanique des Milieux Hétérogènes, ESPCI, Sorbonne Université, UMR CNRS 7635, 7bis quai Saint Bernard, 75231, Paris, France*
[b]*Université Paris-Saclay, CNRS, FAST, Bât. 530, rue André Rivière, 91405, Orsay, France*
[c]*IFREMER, RDT Research and Technological Development Unit, 1625 route de Sainte-Anne, 29280, Plouzané, France*

Abstract

The 3D flying shape of a real-scale 8 m^2 iQFOiL class windsurf sail is measured in steady state sailing configurations. The outdoor conditions are simulated in a large-scale wind tunnel and the flying shape is reconstructed with a stereo camera imaging technique. The twist of the sail profiles is measured simultaneously with aerodynamic forces and moments applied to the sail via an embedded force balance. With the measured forces and moments, the lift, drag and roll coefficients are determined for various wind velocities. A systematic decrease of these coefficients is observed as compared to previous studies on reduced-scale rigid sail model. We suggest that the sail deformation in the wind is crucial to explain these changes.

Keywords: Windsurfing, Sail aerodynamics, Wind tunnel test, Full scale experiment, Fluid-structure interaction, Photogrammetry

1. Introduction

In competitive sailing, the performance of sails is significantly influenced by their structural deformations. Except for some racing classes using rigid wings [1, 2], most sails are flexible structures that continuously interact with

*Corresponding author
Email address: `marc.fermigier@espci.fr` (Marc Fermigier)

the surrounding wind flow, creating complex fluid-structure interaction problems. This complexity is particularly pronounced in highly cambered downwind sails and flexible rigs, such as those found in windsurfing [3, 4]. Windsurf rigs, unlike traditional cruising or racing yachts, are designed without the support of stays and shrouds [5]. They are highly flexible and operate as part of a unified rig, with the integrated mast and boom allowing direct control by the rider. Although windsurf sails themselves are nearly inextensible within typical wind speed ranges, the unsupported and flexible mast leads to significant deformation of the entire rig under wind loading. This unique characteristic makes windsurfing an excellent example of complex fluid-structure interactions, combining technical challenges for competitions. As such, to optimize a sail's aerodynamic efficiency and overall performance under real sailing conditions, it is crucial to obtain precise measurements of its flying shape [6, 7].

Various experimental techniques have been developed to measure the full-scale flying shape of sails under sea sailing conditions. These methods include Time of Flight radar scanning [8], monocular imaging [9], and multiple synchronized cameras combined with both discrete [10, 7, 6, 11] and continuous [12] pattern recognition algorithms. These techniques offer satisfactory accuracy and enable time resolved 3D reconstructions of the flying shape. However, measuring sail shape in steady-state conditions at sea presents challenges due to the inherently unsteady nature of the wind, both in terms of amplitude and direction [13, 14, 8]. To address these challenges, wind tunnel investigations using reduced-scale sail models under controlled wind conditions are commonly employed as alternatives for mainsails [15, 16] or spinnakers [11, 6]. However, such investigations may lead to aerodynamic-structural discrepancies, including mismatched Reynolds numbers as well as variations in the ratios of fabric weight and membrane stress to wind pressure. To our knowledge, full-scale wind tunnel tests of windsurf sails have not yet been reported.

In the context of windsurfing, limited attention has been given to the joint aerodynamic-structural measurements of real-scale windsurf sails. Alexander and Furniss [4] conducted measurements of the aerodynamic coefficients of 1/8-scale rigid models of a Gaastra sail, with the model shapes derived from full-scale sails. Their specifically quantified the reduction in lift coefficient as the sail was flattened and twisted. More recently, Mok *et al.* [17] examined the performance of a 1/4-scale rigid model of an Olympic class iQFOiL sail [18] in a wind tunnel. The model was based on full-scale sail shapes rigged indoors without wind, and the study investigated the effects of rig-back angle and Reynolds number on aerodynamic coefficients by varying the angle of attack between 0° and 70°. In summary, both studies concentrated on aerodynamic efficiency using reduced-scale rigid models. This approach is not fully representative for flexible windsurf sails, whose deformations under wind loading can significantly alter aerodynamic performance.

In the following we present wind tunnel measurements of the aerodynamic coefficients of a full-scale Olympic class iQFOiL sail, based on simultaneous photogrammetric determination of its 3D flying shape. The paper is structured as follows: we begin by detailing the geometric and mechanical characteristics of the sail, including the rigging configurations used. Next, we describe the experimental setup and the wind tunnel testing conditions. We then introduce the two-camera imaging technique employed for flying shape determination, followed by a validation check of the method. Using the reconstructed 3D sail shape data, we quantitatively analyze the sail twist and mast deformation resulting from aerodynamic loading. Finally, along with the simultaneous force measurements, we provide a comprehensive analysis of the sail's flexibility on its aerodynamic performance.

2. Experimental setup

2.1. Sail characteristics

We use a Severne HGO iQFOil 8m^2 sail rigged on an Apex 490 carbon fiber mast which was the approved rigging for women in the 2024 Olympic windsurf class [18]. The mast base is flexibly linked to a Starboard iQFOiL 95 Carbon Reflex board (Fig. 1). The mast (4.9 m long) is slid into a sleeve at the luff (leading edge) of the sail and bent by tensioning the luff with a system of pulleys. The maximum sail chord length C is 2 m.

Seven full battens and 5 battens of reduced length between the 6 upper ones are distributed along the leech (trailing edge) of the sail. The full battens are in compression and bend the sail in an asymmetrical cambered shape, even in the absence of wind. Their tension are adjusted by screws at the trailing edge.

A double-sided carbon fiber boom (wishbone), 2.3 m long, attached to the mast, holds the clew point of the sail with the outhaul line. Adjusting the tension on the outhaul modifies the camber of the sail but also the bending of the whole rig: a large tension on the outhaul flattens the sail and limits the twist of the sail into the wind while a small tension leads to a larger camber and a larger twist. The settings of the sail were checked by a member of the French national Olympic team. In this study, we will use two different outhaul tensions referred to as low camber and high camber.

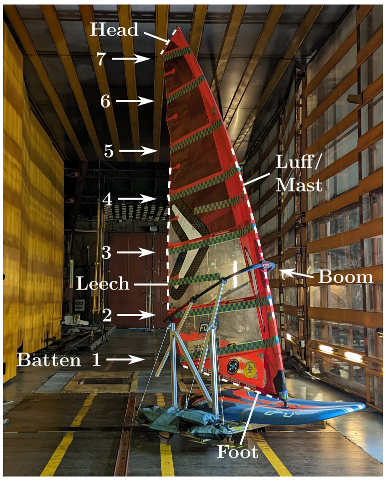

Figure 1: Severne HGO 8 m^2 sail rigged on a 95 v3 Carbon Reflex board and installed in the S6 wind tunnel at IAT Saint-Cyr l'Ecole (France). Green/blue checkerboards are glued on the sail to determine the 3D shape by photogrammetry.

2.2. Wind tunnel

The measurements are carried out in the large low speed S6 wind tunnel at Institut Aérotechnique Saint-Cyr-l'École (France)[1] with a 6 m $\times$ 6 m test section. The tunnel is an open circuit blowdown type with an assembly of 36 fans located 9.6 m upstream of the leading edge of the sail. The wind in the test section is horizontal, unidirectional and mainly constant along the vertical axis. Turbulent intensity is between 4 and 7 % which corresponds to a highly turbulent air flow, but similar to the one observed in sailing conditions [19]. The free-stream wind speed U is varied in the range [4-8] m/s, so the Reynolds numbers of the flow around the sail, $Re = UC/\nu$ based on the maximum chord C, is in the range 0.52×10^6 to 1.04×10^6. Fig. 2a is a sketch of the test bench of the windsurf in the wind tunnel.

[1]`https://iat-en.cnam.fr/`

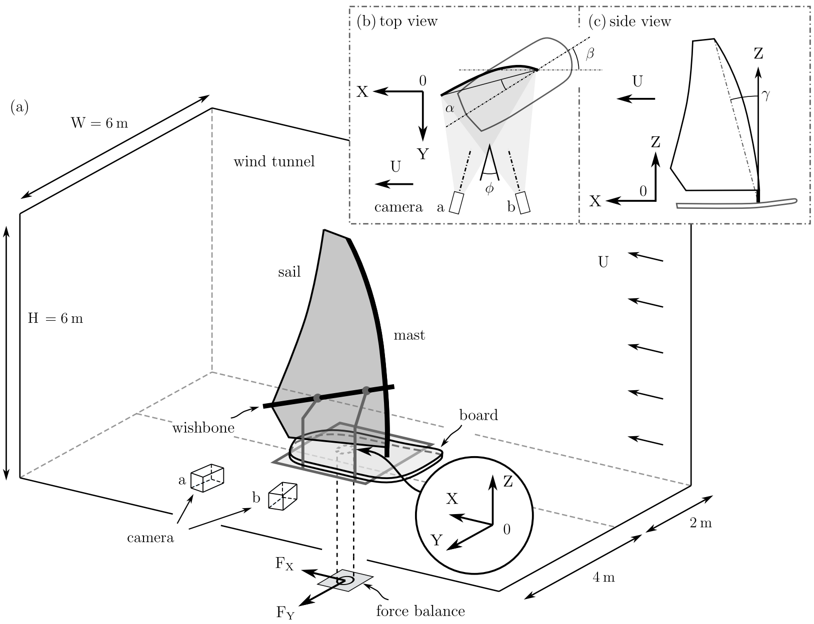

Figure 2: Sketch of the full-scale windsurf in the measuring section of the wind tunnel: (a) perspective view, (b) top and (c) side view. The two cameras are fixed on the high pressure side wall.

The sail is attached to the board using a universal joint, and its orientation is controlled using two ball joints that keep the wishbone in a fixed position (Fig. 1). For our measurements, the wishbone's position is set in a way to keep the mast inclined backwards only with respect to the board with a constant medium rig-back angle $\gamma = 18 \pm 1^\circ$ (Fig. 2c). The board is fixed to a horizontal carriage mounted atop the force balance, which is positioned beneath the wind tunnel floor. The entire board and sail can be rotated around the vertical axis of the balance to vary the wind incidence angle on the sail.

The (X, Y) plane of our coordinate reference system $(0, X, Y, Z)$ is defined as the horizontal plane of the wind tunnel (Fig. 2a). The X axis is the wind flow direction, Z axis points vertically upward and Y axis is perpendicular so that the frame is direct. The origin, 0, is located on the rotating axis of the force balance at the board deck (Fig. 2a).

The force balance is shifted by one meter from the middle of the tunnel to provide a large enough field of view for the cameras (Fig. 2a). The force balance measures 5 components: F_X force component in the direction of wind (i.e. the drag), F_Y horizontal force component perpendicular to the wind direction (i.e. the lift) and M_X, M_Y and M_Z moments around the axis X, Y and Z respectively. The forces and moments are acquired at a rate of 1 kHz and averaged over 20 s.

In order to evaluate the aerodynamic forces and moments on the sail only, the forces and moments on the structure and the board are measured without sail for each measuring point and subtracted from the raw measurements.

Unlike a rigid 3D profile with zero twist, the sail naturally exhibits a vertical twist, which increases with the wind speed. As a result, a clear definition of the angle of attack (AOA) is required. We define an horizontal plane at $Z = 67$ cm, cutting the 3D shape of the sail under the wishbone (between battens 1 and 2, Fig. 1). The AOA is defined as the angle between the chord of this section and the X axis of the coordinate frame. Thanks to the 3D reconstruction of the 3D sail shape, we are able to determine this *in-situ* AOA with a good precision.

To mimic the weight of the rider and to decrease the measured moment M_X, counterweights (60 kg of sandbags) are placed on the upwind side of the assembly that holds the board (Fig. 1). Diminishing this rolling moment M_X is essential to measure accurate values on other components with the dedicated force balance.

2.3. Photogrammetry

We use a stereo photogrammetry technique to determine the 3D shape of the sail. Two synchronized DSLR cameras (Nikon D800, 7360 × 4912 pixels and Nikon D750, 6016 × 4016 pixels, fitted with a Nikon 20 mm $f/2.8$ lens) are mounted on the wall of the tunnel on the pressure side of the sail. The distance between cameras is 4 m and the angle between their optical axes is $\phi = 53.1°$ (Fig. 2a,b).

Blue-green colored checkerboard strips, aligned with the battens, are glued on the sail (Fig. 1) to provide feature points. Additional small checkerboards are positioned on both leech and luff to locate the sail's contour and at the bottom of the mast.

In order to locate automatically the checkerboard corners in each pair of stereo images, we first transform the color images into greyscale images, taking advantage of the contrast between the sail (essentially red) and the checkerboard strips (blue/green) to reduce background contrast. To identify the checkerboard corners we use an algorithm adapted from Duda & Reese [20]: we compute the Radon transform [21] of the image and for each image point we calculate the amplitude of angular variation of the transform. Checkerboard corners are characterized by a large value of this amplitude. Thresholding this amplitude map identifies quite effectively the corners. Based on the pixel positions giving the local maximum amplitude, a Gaussian curve fitting is performed around each position allowing the feature points to be determined with a subpixel resolution. A few spurious detected points are eliminated manually.

Once the checkerboard corners are identified on each camera view, pairing them and using the calibration of the optical space allow us to reconstruct the 3D coordinates of each detected point in the reference frame of the wind tunnel. Given the subpixel resolution of the feature point and a scale factor of 0.91 mm/pixel, the location of the points on the sail is determined with an uncertainty on the order of 1mm in the X and Z directions and a few mm in the Y direction.

3. Measurements of the flying shapes

Using the photogrammetry technique described above, we are able to determine the shape of the sail affected by the aerodynamic load, the so-called flying shape. An example of such a flying shape, measured at a wind speed of 6 m/s, angle of attack of 19.8°, with a high camber, is shown on Fig. 3. In order to characterize the sail shape, we define three vectors: $\mathbf{V_1}$ defined by reference points on the luff and leech between battens 1 and 2. The vector $\mathbf{V_2}$ is located along the top batten and the vector $\mathbf{V_3}$ is located between two reference points on the bottom of the mast (Fig. 3a). The angle between the horizontal component of $\mathbf{V_1}$ and the horizontal component of $\mathbf{V_2}$ defines the global twist of the sail.

A comparison of two measured flying shapes obtained for the same wind speed but a different angle of attack is presented in Fig. 4. Increasing the AOA not only introduces additional twist in the upper part of the sail but also increases the lateral deflection of the mast.

We first focus on the influence of the outhaul tension and of the wind speed on the shape of the sail. To do so, we examine the profile at the level of the 3rd batten. Fig. 5 shows this profile for a fixed angle of attack (AOA = 16.5°), for the two values of outhaul tension and for three values of wind speed

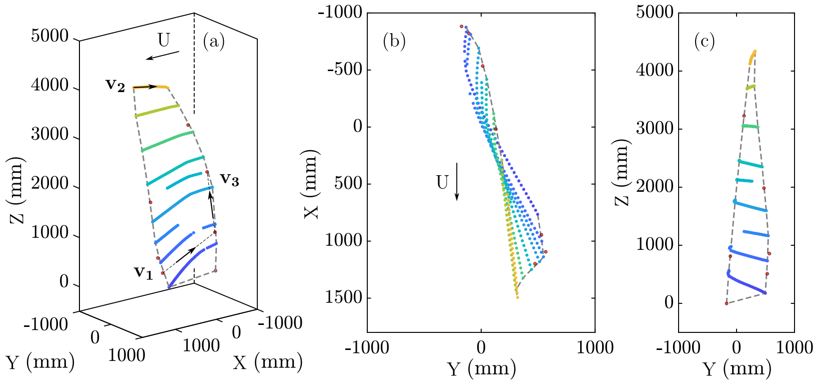

Figure 3: Reconstructed shape of the pressure side of the sail in the coordinate system of the wind tunnel, obtained for U = 6 m/s, AOA = 19.8° and high camber case. The color code from blue to orange represents the value of the Z coordinate. The red dots are the additional reference points on the luff, leech and mast base. (a) 3D perspective view. $\mathbf{V_1}$: vector between luff and leech; $\mathbf{V_2}$: vector along the top batten; $\mathbf{V_3}$: vector along the lower luff. (b) top view (along Z) and (c) rear view (along X).

(4, 6 and 8 m/s). The insets on this figure show details of the profiles at the maximum camber and at the leech (trailing edge). The difference in outhaul tension leads to a 10 mm shift in the position of the trailing edge. When the outhaul tension is reduced, the maximum camber of the sails increases by 10 to 15 mm, depending on the wind speed. The influence of the wind speed on the sail shape can be readily seen as the maximum camber of the sail shifts by several millimeters when the wind increases from 4 to 8 m/s.

Fig. 6 shows the maximum camber A normalized by the chord C of the 3rd batten in percent for all the measured AOA. The grey dashed line corresponds to the AOA = 16.5° selected for Fig. 5. It illustrates the fact that the relative camber evolves of 15 % between the two selected outhaul tensions.

Another impact of fluid structure interaction is the change in sail twist, as shown in Fig. 7. When the sail is rigged on the mast and wishbone, it is already slightly twisted, even without wind due to the compression imposed by the battens. However, as the pressure difference between the two sides of the sail increases, the less constrained top of the sail tends to align with the wind direction. A first evidence from Fig. 4 and Fig. 7 is that the twist increases with the angle of attack (AOA). A larger AOA results in a greater aerodynamic load and increased structural stress on the rig. The rig responds by deforming in its more compliant mode, the torsional mode, with

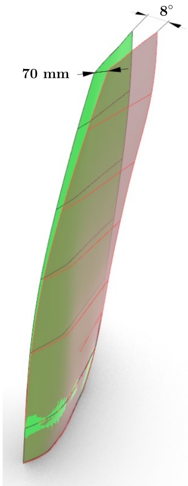

Figure 4: Comparison of two 3D flying shapes of the pressure side of the sail obtained for $U = 8$ m/s in the low camber case: AOA = 1.1° (green) and AOA = 16.1° (red). The bottom of the sail and the bottom part of the mast have been superimposed to highlight the deformation of the top of the sail with the increase of AOA: the twist increases by 8° and the lateral deflection of the masthead by 70 mm.

the secondary mode being the bending of the mast in the plane perpendicular to the wind. For a given AOA, the high camber setting produces a larger twist angle compared to the low camber case, a phenomenon confirmed by practical field experience. In Fig. 7, the continuous line corresponds to a top of the sail aligned with the wind. All measured points fall below this line, indicating that the twist effect reduces the angle of attack but keeps it positive, even at the sail top. Consequently, aerodynamic lift is generated across the entire sail section. Note that two twist angles of the low camber sail are slightly negative for small AOA. This can be attributed to the leech's loose tip, which drops under gravity when aerodynamic forces are low, here with a small negative incidence of the top of the sail.

In addition to the twist, the stress due to the wind induces a lateral deflection of the mast towards the leeward side. This is well known by windsurfers to be highly dependent of the mast top part bending stiffness and to lead to a depower of the sail, but here we can quantify this effect as shown on Fig. 8. To eliminate an overall motion of the rig and take into account only this deformation, we determine the mast head lateral position D_m as the distance

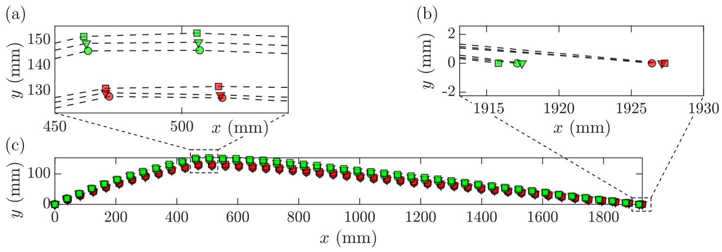

Figure 5: Profile of the 3rd batten for AOA = 16.5° (red: low camber; green: high camber); ◯: $U = 4$ m/s; ▽: $U = 6$ m/s; □: $U = 8$ m/s. (a) Zoom close to the maximum camber, (b) zoom near the trailing edge, (c) global shape. The profiles are represented in a local coordinate $(0, x, y)$ where (0,0) is the front part of the mast (leading edge of the sail), x along the chord of the profile and y in the transverse direction. By this convention, all profiles are rotated around the leading edge and aligned along the chord x for better quantitative comparison.

between the top of the mast and the plane defined by the bottom of the sail (i.e. defined by the two vectors $\mathbf{V_1}$ and $\mathbf{V_3}$ (Fig. 3a)). The evolution of D_m follows the same trend as the twist angle: it increases with AOA and, for a given AOA, it increases with the wind speed and the camber. For example, as illustrated in Fig. 4, the mast head moves 70 mm to the leeward side when the AOA increases from 1.1° to 16.1° at 8 m/s. We can observe a similar mast deformation to the leeward side when the wind goes from 4 to 8 m/s at a constant AOA of 16.5°, an amplitude on the order of 1 % of the mast length.

From this analysis, we understand how the whole rig, sail and mast, deforms. As we report in the following section, this deformability limits the aerodynamic force generated, helping the athletes to sail in strong winds. We expect also a lowering of the point of application of the resulting sail force, thus limiting the capsizing torque.

4. Measurements of the aerodynamic coefficients

Together with the sail shapes, the forces and the moments are simultaneous measured for various wind intensities and directions. Only the lift, drag and rolling moment coefficients are analyzed in the present study. The main effect of the wind intensity is taken into account by dividing these quantities by the dynamic pressure $1/2\rho U^2$ and geometrical parameters which leads to the usual aerodynamic lift, drag and rolling moment coefficients:

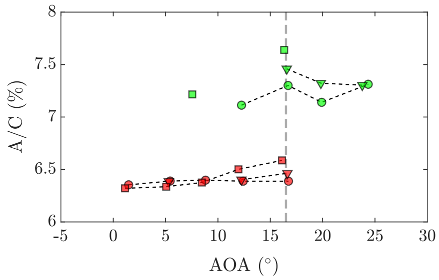

Figure 6: Evolution of the maximum camber A normalized by the reference chord ($C = 2$ m) for the 3rd batten and all the measured AOA (red: low camber; green: high camber); $\bigcirc$: $U = 4$ m/s; $\triangledown$: $U = 6$ m/s; $\square$: $U = 8$ m/s. The grey dashed line corresponds to the AOA = 16.5° selected for Fig. 5.

$$C_L = \frac{F_Y}{\frac{1}{2}\rho U^2 S},\ C_D = \frac{F_X}{\frac{1}{2}\rho U^2 S},\ C_{Mr} = \frac{M_r}{\frac{1}{2}\rho U^2 SC} \tag{1}$$

where U is the free-stream air flow velocity, S the reference sail surface and C the reference chord of the sail. The norm of the rolling moment M_r, is defined as the norm of the moment of the aerodynamic force $M_r = \sqrt{M_X^2 + M_Y^2}$, (*i.e.* not perpendicular to the board or to the sail) where M_X and M_Y are the moments measured in the reference frame of the wind tunnel (Fig. 2 b). We also compute the altitude of the center of application of the rolling force Z_r, dividing the norm of the rolling moment by the norm of the aerodynamic force: $Z_r = M_r/\sqrt{F_X^2 + F_Y^2}$. Measurements of these four quantities, corresponding to both outhaul tensions are shown, for the three wind speeds, on Fig. 9.

Fig. 9a shows a classical behaviour with an increase of the lift coefficient when AOA increases then a decrease when stall occurs. Low camber case (red symbols) induces a slightly larger lift coefficient compared to a high camber (green symbols). This somehow differs with what might be expected of the influence of camber: In the case of thin rigid wings, the asymmetry of the wing and therefore the addition of camber enables the generation of a larger lift force. However taking into account the dynamical deformation of the sail, we have seen that the high camber sail is also more twisted than the small camber one (Fig. 7) so that the highly twisted shape could be responsible for the decrease of lift. In the case of windsurf sails, the outhaul tension has a combined effect on the camber and the global flexibility of the

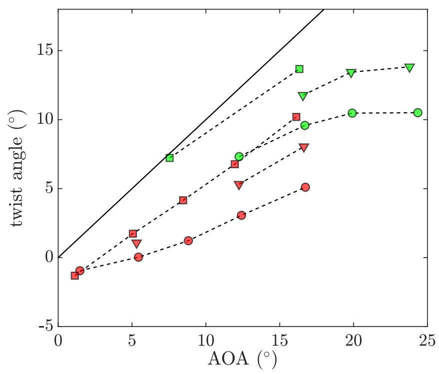

Figure 7: Measured global twist angle of the sail versus the angle of attack (red: low camber; green: high camber; ◯: $U = 4$ m/s; ▽: $U = 6$ m/s; □: $U = 8$ m/s). The black line corresponds to the first diagonal *i.e.* when the top of the sail would be aligned with the wind.

sails. Thus, an higher outhaul tension will reduce the camber but also limit the twist due to the aerodynamic loading. In our case, the effect of twist, directly linked to the evolution of AOA along the span, has a greater impact on the aerodynamic performance than the section profile itself, namely the camber.

On the other hand, our data reveal also a wind speed influence on the lift coefficient. For a given AOA, C_L decreases with increasing wind speed for both cases. Generally speaking, in high turbulent flow regimes such as is our case ($Re = 5.1 \times 10^5 - 1.0 \times 10^6$), C_L is expected to be insensitive to Re. This sensitivity in wind speed suggests that the sail's 3D deformability must come into play. Contrary to a rigid airfoil with an AOA independent of the spanwise coordinate, the twisted sail profile results in an AOA decreasing from bottom to top. This twist angle being the result of a balance between the wind dynamic pressure and the elastic stresses within the rigging structure, alters also with the wind speed. A higher wind speed leads to a higher twist of the sail, a smaller local AOA and thus a smaller C_L. This argument is supported by comparing with experimental data of a 1/4 reduced-scale twist-free rigid sail model, at a similar yet smaller Reynolds number, by Mok *et al.* [17] (black dots). The difference is however smaller at small AOA, possibly because at small incidence angles forces are smaller and thus deformations too. The sail twist also induces a stall delay, from around 17° for the twist-free rigid sail model, to 20° in our case.

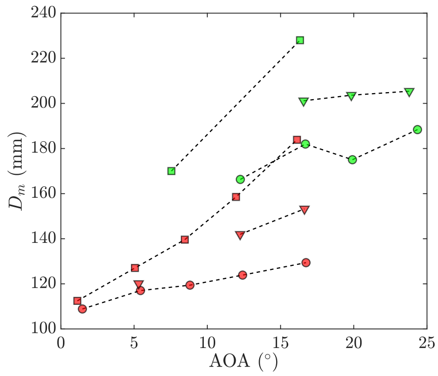

Figure 8: Lateral position of the mast head D_m compared to plane defined by the lower part of the sail, as a function of AOA and for different wind speeds and cambers (red: low camber; green: high camber; $\bigcirc$: $U = 4$ m/s; $\bigtriangledown$: $U = 6$ m/s; $\square$: $U = 8$ m/s).

The presence of an obstacle in the measurement section of a wind tunnel causes an acceleration of airflow on both sides, known as the blockage effect [22]. This effect can alter the aerodynamic and structural measurements of the sail and is usually quantified by the blockage ratio, which is the ratio of the obstacle projected area to the cross-sectional area of the wind tunnel. If the blockage ratio is less than 10 %, the additional effect can be considered negligible [23, 24]. Given the projected area of the sail at a large angle of attack (AOA) of 25°, the blockage ratio is calculated to be 9 %. Thus, we will neglect this blockage effect in the following. Another effect to consider for the lift on a sail or a wing is the wall effect. A small distance between the wall and the suction side of the sail can induce additional lift and drag [25, 26]. In our study, the sail was shifted towards the wall to optimize the cameras' field of view, resulting in a 2 m distance between the suction side of the sail and the wall for a sail chord of 2 m. To estimate this effect, we used Rosenhead's analysis of potential flow around an inclined 2D flat plate confined between two walls. Based on our data, the additional lift accounts for 33 % of the total measured lift at an angle of attack (AOA) of 25° and should not be neglected. However, these analytical estimations are based on a 2D profile using a potential flow approach, which clearly fails to account for the complexities of a 3D sail, especially with twisted profiles that result in varying AOA along the sail's vertical positions in turbulent flow. In our study, we present the results obtained directly from the force and moment

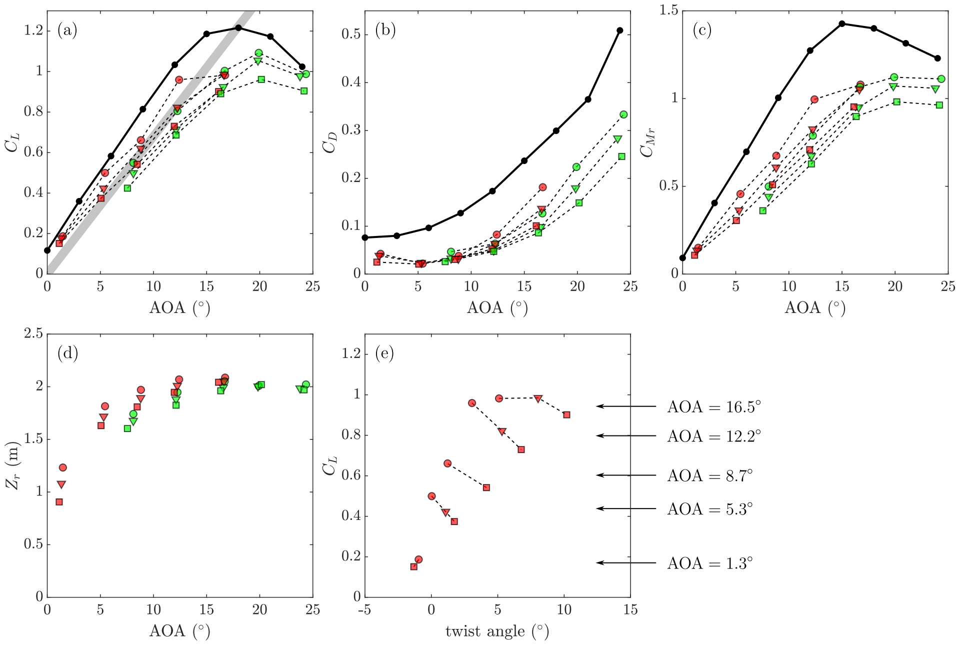

Figure 9: Evolution of the aerodynamic coefficient with AOA: (a) lift coefficient C_L (the grey shaded bar corresponds to the classical prediction for a finite span thin symmetrical profile with elliptical loading $C_L = 2\pi\lambda/(\lambda+2) \times AOA$, where $\lambda = 3.36$ is the present sail aspect ratio), (b) drag coefficient C_D, (c) Rolling moment coefficient C_{Mr} and (d) altitude of the centre of pressure Z_r. (e) Evolution of the lift coefficient C_L as a function of twist angle for selected values of the AOA. Red symbols are for low camber; green for high camber; $\bigcirc$: $U = 4$ m/s; $\bigtriangledown$: $U = 6$ m/s; $\square$: $U = 8$ m/s. Black dots and thick continuous black line are corresponding data from [17].

measurements without applying further non-validated corrections.

Data of the drag coefficient are shown in Fig. 9b. For small wind speeds (AOA $< 10°$), all measured data for both rig settings collapse onto a single curve and reach a minimum around 6° for the low camber case. Above AOA $= 10°$, C_D increases with increasing AOA.

The data dispersion in wind speed for C_D is more pronounced than for C_L. C_D decreases with increasing speed and a maximum reduction of 39 % is found at AOA $= 20°$ between the two extreme wind speeds. As mentioned for the C_L values, a higher wind speed leads to a higher twist and the sail's upper part becomes more aligned to the air flow direction thus reducing the drag. However, when compared with those of the 1/4 twist-free rigid model, the present values of C_D are surprising small and even smaller in some cases than the minimum possible value corresponding to the induced drag of a wing with an elliptic lift distribution [27]. We can't rule out the possibility of errors in the process of subtracting the drag on the structure and on the board or errors induced by large transverses values and an imperfect diagonalization of the measures of the force balance.

The roll moment coefficient C_{Mr} is shown in Fig. 9c. Similar trends as for C_L are observed: a decrease of the coefficient when the wind speed or the camber increase. Probably for the same reason as for Fig. 9b, values are smaller than in [17].

To highlight the influence of the sail deformation on the roll moment, we also plot on Fig. 9d the altitude Z_r of the center of effort. We see that data for both cambers follow a similar trend with AOA. At higher AOA, all data converge to a height of 2 m approximately, suggesting that the effect of camber vanishes at large wind angles and that the stall-induced lift loss has little impact on Z_r. At smaller AOA, the low camber case leads to a larger Z_r as compared to the high camber case. The difference reads 20 cm at the optimal AOA around 10°. Except at large AOA, an increase in wind velocity leads to a decrease of Z_r as expected from the enhanced twist. This highlights again the self-adjustment of deformable rigs allowing the athletes to sail in strong winds.

Finally, Fig. 9e illustrates the variation of lift coefficients as a function of twist angle, for the case of low camber. A general positive correlation between the lift coefficient C_L and twist angle is observed, but it corresponds to the correlation between twist and AOA which increases here from 1.3° to 16.5°. Indeed for a constant AOA, increasing wind speed results in a negative correlation between C_L and twist angle: higher wind speeds induce greater twist angles. At the highest AOA of 16.5°, this effect seems to decrease, likely due to stall occurrence.

5. Discussion

Due to the finite width of the wind tunnel, the measurement of the flying shapes was conducted only on the pressure side surface of the sail. The suction side has not the same shape close to the mast, as the sail is made there of a double skin that surrounds the mast. It is only further downwind that the sail becomes a single layer of Mylar. However, the measurement of the pressure side surface alone is an effective method of highlighting the deformations in the sail caused by the flow.

In real sailing condition, the wind is not of constant velocity in the first meters above the sea level because of the turbulent atmospheric boundary layers. In consequence, as the board moves in a different direction than the wind, the apparent wind in the frame of the board is not of constant direction and constant intensity with Z: it is twisted and the AOA increases with altitude for a non twisted profile. This effect can be as large as 5° for a windsurf sailing upwind at 15 knots in a true wind of 15 knots. Apparent wind twist, which depends on boat speed, is quite difficult to simulate in a wind tunnel [28, 29]. It should logically increase the sail twist observed at sea compared to wind tunnel measurements.

In this study we coupled measurements of the shape of the sail with measurements of the associated aerodynamic forces. We see through analyses on lift force, drag force and roll moment the significant effects of the sail twist on the sail performance. Fluid-Structure Interaction on the windsurf sail result in an increase of the twist along the span and a mast deflection on the leeward side. Both the twist and mast deflection have an impact on the aerodynamic performance of the sail, especially by decreasing the local AOA of the upper section of sail, thus decreasing the force generated in the top. Not considering this deformation using a rigid shape could lead to an overestimation of the lift coefficient of more than 20%. Both large camber and large wind speed lead to an increase in sail twist, an effect that cannot be analyzed with rigid sail measurement. Concerns have been raised regarding the measurement of drag forces, which yielded values of aerodynamic lift to drag ratio that look too large when compared to existing literature.

6. Conclusion

A full scale Olympic windsurf sail has been tested in a wind tunnel. A three-dimensional sail shape reconstruction system has been developed, based on a method of stereophotography detection of points by the Radon transform. The global estimated resolution is on the order of a few millimeters. The effect on sail deformation of various sailing condition and sail parameters was tested, including flow speed, angle of attack, and sail tension settings at the clew. These shape measurements were coupled with drag force, lift force, and roll moment measurements to determine aerodynamic performance, taking into account Fluid-Structure Interactions. It was observed that Fluid-Structure Interactions significantly affect the aerodynamic performance of the windsurf sail mostly by twisting the structure with the effect of reducing the local AOA at the top part of the sail, thus the lift generated. It was shown that the outhaul tension which is commonly used to modify the camber of the sail has also an impact of the global flexibility of the sail. A higher tension in the outhaul will indeed constrain the structure and then limit the twisting of the upper part of the sail. Our main message is that Fluid-Structure Interaction must be explicitly taken into account when testing or simulating such deformable riggings.

Acknowledgments

We thank Louis Giard, member of the French national sailing team, for rigging and adjusting properly the sail shape as well as Pierre Noesmoën, national windsurf coach for fruitful discussions. We thank Clodoald Robert and the technical staff of IAT, as well as Paul Iachkine from the Ecole Nationale de Voile et des Sports Nautiques for their help during the measurements.

This work was supported by the French National Research Agency with grant "Sport de Très Haute Performance" ANR 19-STHP-0002.

References

[1] A. Fiumara, N. Gourdain, V. Chapin, J. Senter, Y. Bury, Numerical and experimental analysis of the flow around a two-element wingsail at reynolds number 0.53×106, International Journal of Heat and Fluid Flow 62 (2016) 538–551. doi:https://doi.org/10.1016/j.ijheatfluidflow.2016.08.005.

[2] A. Hillenbrand, L. M. Giovannetti, U. Dhomé, J. Kuttenkeuler, Wind tunnel tests of a two-element wingsail with focus on near-stall aerodynamics, Journal of Sailing Technology 9 (01) (2024) 110–127. doi:10.5957/jst/2024.9.1.110.

[3] S. Fagg, The development of a reversible and finitely variable camber windsurf fin, Ph.D. thesis, Bournemouth University (1997).

[4] K. Alexander, V. Furniss, Systematic measurements of a windsurfer sail performance, in: 13th Australasian Fluid Mechanics Conference, 1998, pp. 499–502.

[5] P. Hart, Windsurfing, Crowood, 2014.

[6] N. Aubin, B. Augier, J. Deparday, M. Sacher, P. Bot, Performance enhancement of downwind sails due to leading edge flapping: A wind tunnel investigation, Ocean Engineering 169 (2018) 370–378.

[7] J. Deparday, P. Bot, F. Hauville, B. Augier, M. Rabaud, Full-scale flying shape measurement of offwind yacht sails with photogrammetry, Ocean Engineering 127 (2016) 135–143.

[8] F. Fossati, I. Bayati, F. Orlandini, S. Muggiasca, A. Vandone, G. Mainetti, R. Sala, C. Bertorello, E. Begovic, A novel full scale laboratory for yacht engineering research, Ocean Engineering 104 (2015) 219–237.

[9] L. Maciel, R. Marroquim, M. Vieira, K. Ribeiro, A. Alho, Monocular 3d reconstruction of sail flying shape using passive markers, Machine Vision and Applications 32 (2021) 1–22.

[10] G. Clauss, W. Heisen, Cfd analysis on the flying shape of modern yacht sails, in: Proceedings of the 12th International Congress of the International Maritime Association of the Mediterranean. Lisbon, 2005, pp. 87–94.

[11] K. Graf, O. Müller, Photogrammetric investigation of the flying shape of spinnakers in a twisted flow wind tunnel, in: SNAME Chesapeake Sailing Yacht Symposium, SNAME, 2009, p. D021S002R001.

[12] J. Mausolf, J. Deparday, K. Graf, H. Renzsch, C. Böhm, Photogrammetry based flying shape investigation of downwind sails in the wind tunnel and at full scale on a sailing yacht, in: SNAME Chesapeake Sailing Yacht Symposium, SNAME, 2011, p. D011S001R003.

[13] I. Viola, R. Flay, Sail pressures from full-scale, wind-tunnel and numerical investigations, Ocean Engineering 38 (2011) 1733–1743.

[14] J. Deparday, P. Bot, F. Hauville, D. Motta, D. Le Pelley, R. G. Flay, Dynamic measurements of pressures, sail shape and forces on a full-scale spinnaker, in: The 23rd International HISWA Symposium on Yacht Design and Yacht Construction, 2014, p. 13.

[15] F. Fossati, S. Muggiasca, I. M. Viola, Wind tunnel techniques for investigation and optimization of sailing yachts aerodynamics, in: 2nd High Performance Yacht Design Conference, 2006, pp. 105–113.

[16] M. Sacher, F. Hauville, R. Duvigneau, O. Le Maître, N. Aubin, M. Durand, Efficient optimization procedure in non-linear fluid-structure interaction problem: Application to mainsail trimming in upwind conditions, Journal of Fluids and Structures 69 (2017) 209–231.

[17] K. P. Mok, P. Zhou, J. Hou, S. Zhong, X. Zhang, R. C.-H. So, K. Y. Chan, Performance of a windsurfing sail under steady condition, Ocean Engineering 289 (2023) 116295.

[18] H. Gonzalo, Costa, 2023 Annual Report IQFoil Class Association, in: IQFoil Class Association, World Sailing, 2023, pp. 1–2.

[19] R. B. Stull, An introduction to boundary layer meteorology, Vol. 13, Springer Science & Business Media, 2012.

[20] A. Duda, U. Frese, Accurate detection and localization of checkerboard corners for calibration, in: British Machine Vision Conference, 2018, pp. 1–10.
URL `https://api.semanticscholar.org/CorpusID:52286128`

[21] J. Radon, 1.1 über die bestimmung von funktionen durch ihre integralwerte längs gewisser mannigfaltigkeiten, Classic papers in modern diagnostic radiology 5 (21) (2005) 124.

[22] J. B. Barlow, W. H. Rae, A. Pope, Low-speed wind tunnel testing, John wiley & sons, 1999.

[23] D. A. Spera, Wind turbine technology, Fairfield, NJ (United States); American Society of Mechanical Engineers, 1994.

[24] T. Chen, L. Liou, Blockage corrections in wind tunnel tests of small horizontal-axis wind turbines, Experimental Thermal and Fluid Science 35 (3) (2011) 565–569.

[25] L. Rosenhead, The lift on a flat plate between parallel walls, Proc. Roy. Soc. A132 (1931) 127.

[26] A. Green, The two-dimensional aerofoil in a bounded stream, The Quarterly Journal of Mathematics 18 (1) (1947) 167–177.

[27] J. D. Anderson, M. L. Bowden, Introduction to flight, Vol. 582, McGraw-Hill Higher Education New York, NY, USA, 2005.

[28] R. G. Flay, A twisted flow wind tunnel for testing yacht sails, Journal of Wind Engineering and Industrial Aerodynamics 63 (1-3) (1996) 171–182.

[29] P. Richards, The effect of wind profile and twist on downwind sail performance, Journal of wind engineering and industrial aerodynamics 67 (1997) 313–321.